

Stochastic Bursting Analysis of an Extended Morris Lecar Neuron

Yatin Prakash

December 21, 2025

Abstract

Neuronal bursting plays a critical role in neural coding, rhythmic activity, and signal amplification across the central nervous system. The generation of high-frequency spike clusters separated by quiescent intervals is a signature of many excitable neurons, including thalamic relay, cortical pyramidal, and cerebellar neurons. The classic Morris–Lecar (ML) model captures the essence of excitability but lacks the slow feedback necessary to explain bursting.

This project develops simple theoretical extensions and creates a modified ML neuron model that integrates intracellular calcium dynamics and stochasticity to reproduce and understand physiologically observed bursting behaviour. Using a nonlinear dynamical systems approach, we couple membrane voltage and K^+ gating variables to a slow calcium component through a calcium-activated potassium current (I_{KCa}). Numerical simulations and phase-plane analysis are used to understand square-wave and elliptic bursting patterns. Key parameters—the calcium clearance rate (ε), calcium-activated potassium conductance (g_{KCa}), and noise intensity (σ)—are found to systematically tune burst duration, inter-burst interval, and temporal coherence and can be extended to ideas like resonance.

This minimal yet biologically relevant model bridges cellular neurophysiology and nonlinear dynamical theory, offering interpretable parameters that link calcium signaling to neural excitability and rhythmic pattern formation common in many neural circuits. The model provides a reproducible foundation for exploring modulated bursting in other excitable systems and can serve as a framework for neuronal niche simulation.

Contents

1 A Primer to the Morris-Lecar System	1
1.1 The Dynamical System	2
1.2 Type I and II Spiking in ML	4
1.3 Discussions	6
2 Introduction to Bursting	8
3 Square-Wave Burster	8
3.1 Understanding Geometric Structure	10
3.2 Methods and Observations	10
4 Elliptic Burster	13
4.1 Classification: Hard vs. Soft Elliptic Bursting	13
5 Appendix	13

1 A Primer to the Morris-Lecar System

The Morris–Lecar (ML) model is a reduced two-dimensional conductance-based model of an excitable neuronal cell membrane. Originally introduced in 1981 by Kathleen Morris and Harold Lecar to describe voltage oscillations in the giant muscle fiber of the barnacle, *Balanus nubilus* [5], the model utilizes voltage-clamp data to describe ionic currents through calcium (Ca^{2+}) and potassium (K^+) channels. The excitable membrane is conceptualized as an electrical circuit. The lipid bilayer acts as a capacitor, while ion channels act as variable resistors. General features of the system are (a) a propensity to produce damped or sustained oscillations over a rather broad parameter range, and (b) For cells subject to changeable parameters a system dominated by two noninactivating conductances can exhibit varied oscillatory and bistable behavior.[5]

The spikes can be described by the following sequence of events:

- **Depolarization:** Ca^{2+} ions flow into the cell, driving the membrane potential V toward positive values.

- **Repolarization:** K^+ ions flow out of the cell, driving V back toward the negative resting potential.
- **Leak:** A passive leak current maintains the resting steady state. These may include other current channels that are (assumed) not dominant in determining the excitability.

The power of the Morris–Lecar model lies in its dimensionality reduction. It serves as a canonical model, offering a bridge between complex, high-dimensional biophysical models (like Hodgkin–Huxley; extended to 5 dimensions or more) and abstract mathematical models (like Integrate-and-Fire; one dimensional assumes all or none firing), alongside other reduced models such as the Izhikevich and Hindmarsh–Rose models.^[4] This reduction allows for complete phase-plane analysis, making it possible to visualize the geometry of excitability and exhibits both classes I and II excitabilities when system parameters are set appropriately.

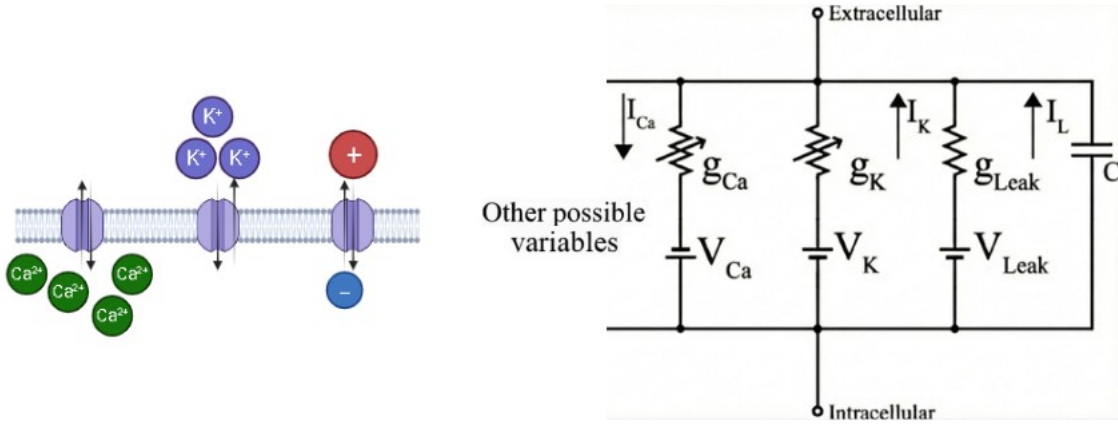


Figure 1: Representations of ion flow across a neuronal membrane and an equivalent circuit diagram. The leak channel is not selective for a single ion species. The direction of ionic current through the channel can be inward or outward depending on the electrochemical driving force.

1.1 The Dynamical System

The model is governed by conservation of current equation.

The total current crossing the membrane is the sum of the capacitive current and the ionic currents.

$$C \frac{dV}{dt} = I_{\text{app}} - I_{\text{ion}}(V, w), \quad (1)$$

$$\frac{dw}{dt} = \phi \frac{w_\infty(V) - w}{\tau_w(V)}, \quad (2)$$

For the Ca^{2+} current, we assumed instantaneous activation, meaning $m_\infty(V)$ is in a steady state and we do not need a dm/dt equation. The total ionic current I_{ion} is given by:

$$I_{\text{ion}}(V, w) = \underbrace{g_{Ca} m_\infty(V)(V - E_{Ca})}_{Ca^{2+} \text{ Depolarising Current}} + \underbrace{g_K w(V - E_K)}_{K^+ \text{ Hyperpolarising Current}} + \underbrace{g_L(V - E_L)}_{\text{Leak Current}}. \quad (3)$$

There are three kinds of ion-channels: a K^+ , a leak, and Ca^{2+} channels.

Where g_K is maximum conductance and w is an activation variable, the fraction of open K^+ channels. w approaches its equilibrium value, $w_\infty(V)$, with a rate of $\tau_w^1(V)$, where $\tau_w = \tau_w(V)$ is the so-called time constant.

Steady-State Functions and Kinetics

The gating variables assume a Boltzmann (sigmoidal) distribution for their steady-state activation:

$$m_\infty(V) = \frac{1}{2} \left[1 + \tanh \left(\frac{V - V_1}{V_2} \right) \right], \quad (4)$$

$$w_\infty(V) = \frac{1}{2} \left[1 + \tanh \left(\frac{V - V_3}{V_4} \right) \right]. \quad (5)$$

The voltage-dependent time constant for the w variable is modeled as:

$$\tau_w(V) = \frac{1}{\cosh\left(\frac{V-V_3}{2V_4}\right)}. \quad (6)$$

Refer the table for a detailed variable description and key assumptions.

Table 1: Model Description

Symbol	Description
$v(t)$	Membrane voltage (mV). Primary dynamic variable.
$n(t)$	Potassium activation variable (dimensionless). Controls K^+ current.
$m(t)$	Calcium activation variable (dimensionless). Controls Ca^{2+} current.
C	Membrane capacitance ($\mu F/cm^2$). Governs rate of voltage change.
i	Applied external current ($\mu A/cm^2$). Assumed nonnegative.
g_L	Leak conductance (mS/cm^2). Voltage-independent passive current.
g_{Ca}	Maximum calcium conductance (mS/cm^2). Scales inward Ca^{2+} current.
g_K	Maximum potassium conductance (mS/cm^2). Scales outward K^+ current.
E_L	Leak reversal potential (mV). Resting passive equilibrium voltage.
E_{Ca}	Calcium reversal potential (mV). Large positive value.
E_K	Potassium reversal potential (mV). Large negative value.
$m_\infty(v)$	Steady-state calcium activation: $\frac{1}{2} \left[1 + \tanh\left(\frac{v-v_1}{v_2}\right) \right]$.
$n_\infty(v)$	Steady-state potassium activation: $\frac{1}{2} \left[1 + \tanh\left(\frac{v-v_3}{v_4}\right) \right]$.
$\tau_n(v)$	Voltage-dependent time constant for n : $\frac{1}{\cosh\left(\frac{v-v_3}{2v_4}\right)}$.
τ_m	Time constant for calcium activation variable m .
ϕ	Scaling factor for the speed of n -dynamics.
v_1, v_2	Half-activation voltage and slope factor for $m_\infty(v)$.
v_3, v_4	Half-activation voltage and slope factor for $n_\infty(v)$.

Moreover the following constraints are assumed on the parameter space:

* g_L , g_{Ca} and g_K are always positive. E_L , $E_K < 0$ and $E_{Ca} > 0$ so that $E_K < E_L < E_{Ca}$. The applied current, i , is always nonnegative.

* **Instantaneous Ca^{2+} Activation:** The model assumes the calcium channels respond so rapidly to voltage changes that their activation variable m is always at steady state ($m = m_\infty(V)$). Ca^{2+} current does not inactivate in the classical model. Repolarization relies entirely on the activation of K^+ .

*Slow K^+ Dynamics The potassium channels operate on a slower timescale, necessitating the differential equation for w .

Because the system is two-dimensional, we can determine the global behavior [7] of the neuron by plotting the variables V against w . The trajectory of the system $(V(t), w(t))$ is dictated by the **nullclines**.

The nullclines are the curves obtained by setting the first derivatives to zero. This curve defines the set of points where the membrane potential does not change. The table below demonstrates the physical meaning of these curves:

Solving Eq. (1) for w yields:

$$w = \frac{I_{app} - g_{Ca}m_\infty(V)(V - E_{Ca}) - g_L(V - E_L)}{g_K(V - E_K)}. \quad (7)$$

Let (V^*, w^*) be the points where $\dot{V} = 0$ and $\dot{w} = 0$. More generally, in a higher-dimensional system the stability of these points is determined by the eigenvalues of the Jacobian matrix J evaluated at (V^*, w^*) . For our purposes in the 2D model, the local stability of an equilibrium is fully determined by the trace and determinant of the Jacobian matrix evaluated at that point.

Table 2: Nullcline Description

V-Nullcline ($\dot{V} = 0$)	w-Nullcline ($\dot{w} = 0$)
Shows the membrane voltages at which the <i>total ionic current</i> is zero. Determined by Ca^{2+} , K^+ , and leak currents.	Shows the voltages at which the recovery variable w does not change. Defined by potassium gating variable $w = w_\infty(V)$.
Forms a nonlinear “N-shaped” curve because Ca^{2+} current depends on both the activation function $m_\infty(V)$ and the driving force ($V - E_{\text{Ca}}$).	Forms a smooth, monotonically increasing sigmoid that reflects slow recovery kinetics.
* Left branch: stable resting state. * Middle branch: unstable threshold region. * Right branch: depolarized excited state.	Steepness and horizontal shift are set by V_3 and V_4 , which govern the voltage sensitivity and slope of the gating kinetics.
The shape and intersections jointly determine excitability, oscillations, and bistability.	
Represents fast voltage dynamics.	Represents slow recovery dynamics.
Controls excitability transitions.	Controls return to equilibrium.
Intersection: The crossing of the V - and w -nullclines gives the system’s <i>fixed points</i> . These intersections provide a geometric picture of how voltage and recovery dynamics jointly determine neuronal behavior.	

We have Hartman-Grobman Theorem that says that in the neighborhood of an equilibrium the flow of the nonlinear system can be approximated accurately using a linear system. Because the characteristic equation of a 2×2 Jacobian is quadratic,

$$\lambda^2 - (\text{tr} J)\lambda + \det J = 0, \quad (8)$$

according to our equations:

$$J = \begin{pmatrix} \frac{\partial \dot{V}}{\partial V} & \frac{\partial \dot{V}}{\partial w} \\ \frac{\partial \dot{w}}{\partial V} & \frac{\partial \dot{w}}{\partial w} \end{pmatrix}. \quad (9)$$

The signs of $\text{tr}(J)$ and $\det(J)$ are sufficient to determine the real parts of the eigenvalues. Thus, explicit computation of eigenvalues is unnecessary:eigenvalues add no further information. The trace–determinant pair encodes all information required for local linear stability analysis in two-dimensional models.In the code I numerically find V^* using sign changes and *brentq*; Remaining is similar to that described below. This table summarises the procedure to determine stability of points.

Table 3: Summary of Stability Analysis in the Morris–Lecar Model

Concept	Summary
Equilibria	Solve $\dot{V} = 0$ with $w = w_\infty(V)$ to find V^* ; set $w^* = w_\infty(V^*)$.
Jacobian Computation	Linearize the system at (V^*, w^*) using the Jacobian.
Trace–Determinant Method	For 2D systems, stability is fully determined by $\text{tr}(J)$ and $\det J$. 1. $\det J < 0$: saddle. 2. $\det J > 0$, $\text{tr} J < 0$: stable. 3. $\det J > 0$, $\text{tr} J > 0$: unstable. Where, $\text{tr}(J) = \lambda_1 + \lambda_2, \quad \det(J) = \lambda_1 \lambda_2.$
NOTE: The discriminant $\Delta = (\text{tr} J)^2 - 4 \det J$ indicates whether a 2D equilibrium is a node (real eigenvalues) or a spiral/focus (complex eigenvalues), complementing the trace and determinant in determining local stability.(We do not use this in our analysis)	

1.2 Type I and II Spiking in ML

This simple model shows different types of dynamics such as hopf bifurcation, saddle node on invariant circle (SNIC) limit cycles and homoclinic bifurcation. See appendix fo rthe different parameters that cause these transitions.The I_{app} parameter is varied

in our study. As a supplement, this project also develops a simple model to study these phenomenon. The set of diagrams below aim to capture the essence of these bifurcations.

Class I and Class II excitability parameters To reproduce these behaviors, standard parameter sets are used (adapted from [6] and [3]).

Table 4: Standard Morris–Lecar Parameter Sets ($C = 20 \mu\text{F}/\text{cm}^2$). Note the difference in V_3 and V_4 , which shifts the dynamics from Class I to Class II.

Parameter	Symbol	Class I (SNIC)	Class II (Hopf)	Units
Ca ²⁺ Conductance	g_{Ca}	4.0	4.4	mS/cm^2
K ⁺ Conductance	g_K	8.0	8.0	$\text{mS}/\text{cm}^2\text{g}$
Leak Conductance	g_L	2.0	2.0	mS/cm^2
Ca ²⁺ Potential	E_{Ca}	120	120	mV
K ⁺ Potential	E_K	-84	-84	mV
Leak Potential	E_L	-60	-60	mV
Ca ²⁺ Half-Act.	V_1	-1.2	-1.2	mV
Ca ²⁺ Slope	V_2	18.0	18.0	mV
K ⁺ Half-Act.	V_3	12.0	2.0	mV
K ⁺ Slope	V_4	17.4	30.0	mV
Kinetic Scale	ϕ	0.067	0.04	—

The middle branch of the V nullcline is the impulse threshold. Such qualitative change in behavior is called a bifurcation, and this particular bifurcation is called a Hopf bifurcation. Anequilibrium or steady state is considered locally stable if the phase point returns to the equilibrium if perturbed away by a small amount. This is regardless of the exact perturbation (i.e., the direction of perturbation in the phase space), as long as it is not a large perturbation.

Some neurons exhibit type 1 dynamics, so the firing rate declines to near 0 as the applied current is decreased. Other neurons exhibit type 2 dynamics, so the system makes an abrupt transition from continuous spiking to rest as the applied current is decreased.

Table 5: Sequence of events for Type 1 (Integrator) Morris–Lecar model

I_{app}	Location	Bifurcation/Stability	Behavior
Low	Left branch	Stable Node	Resting State
↗	Toward knee	Attraction weakens	Increased excitability
Threshold	At lower knee	SNIC	Fixed point vanishes
Moderate	(No left FP)	Stable limit cycle	Tonic spiking
↗	—	—	Frequency increases
High	Right branch	Unstable spiral (via SubHopf)	Spiking continues
Very High	Right branch	Stable (via SuperHopf)	Depolarization block

Table 6: Sequence of events for Type 2 (Resonator) Morris–Lecar model

I_{app}	Location	Bifurcation/Stability	Behavior
Low	Left branch	Stable node or focus	Resting state
Threshold	Near left knee	Subcritical Hopf (unstable LC appears)	Increased excitability; oscillatory tendency
Moderate	Right branch (no stable FP)	Stable limit cycle (post–SubHopf)	Tonic spiking with finite onset frequency
Higher	Right branch	Stable limit cycle persists	Spiking continues; frequency increases
Very High	Far right branch	Stable equilibrium (via saddle-node of cycles or supercritical Hopf)	Depolarization block (high-voltage steady state)

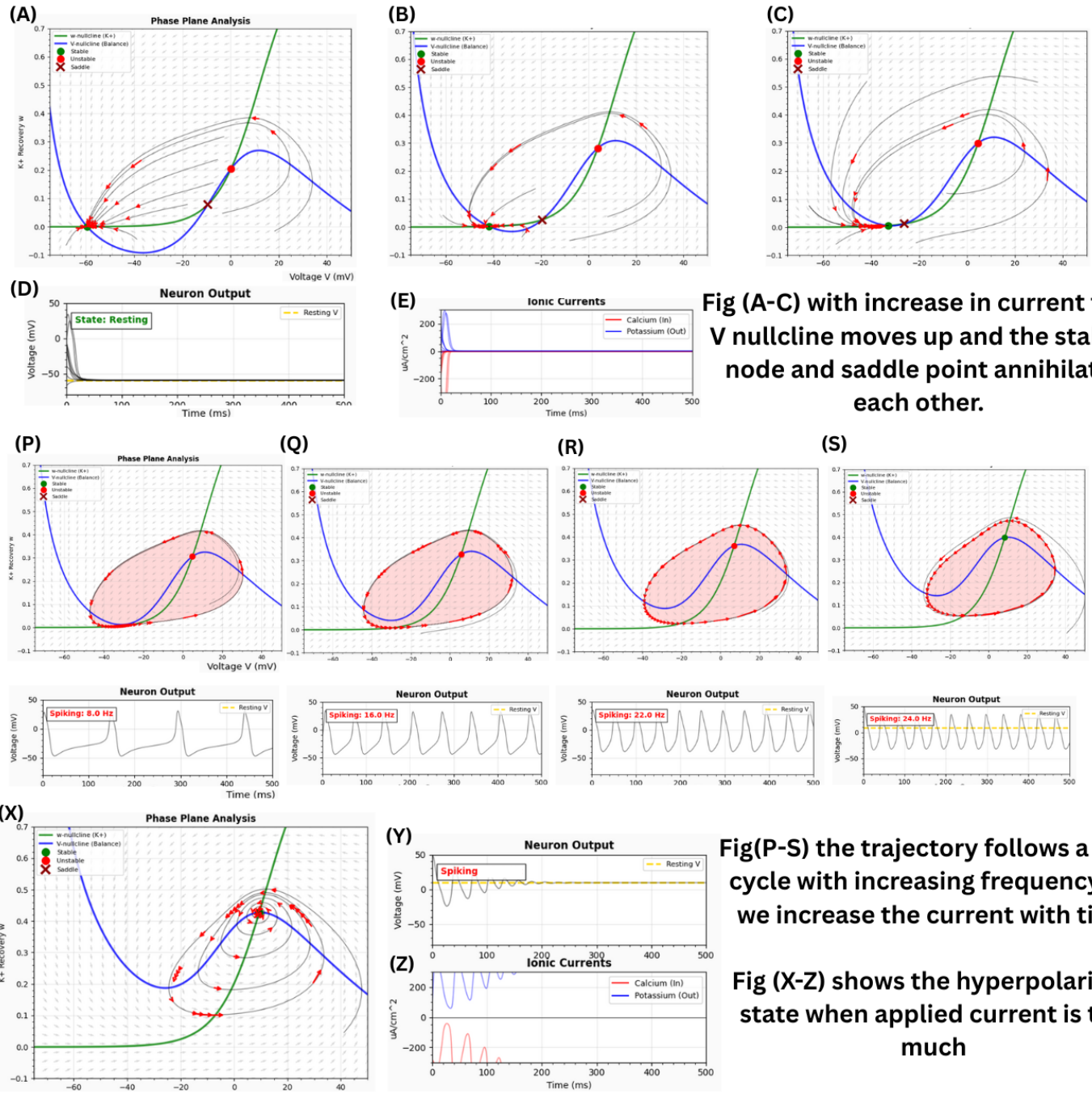


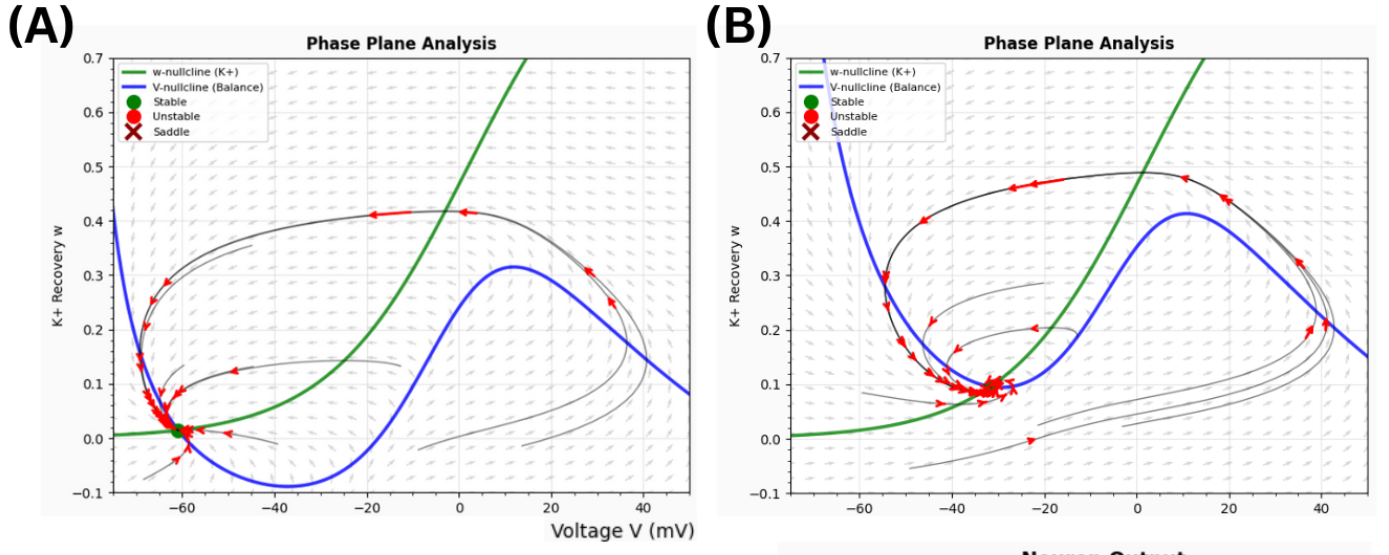
Figure 2: Schematic representation of Type 1 dynamics

1.3 Discussions

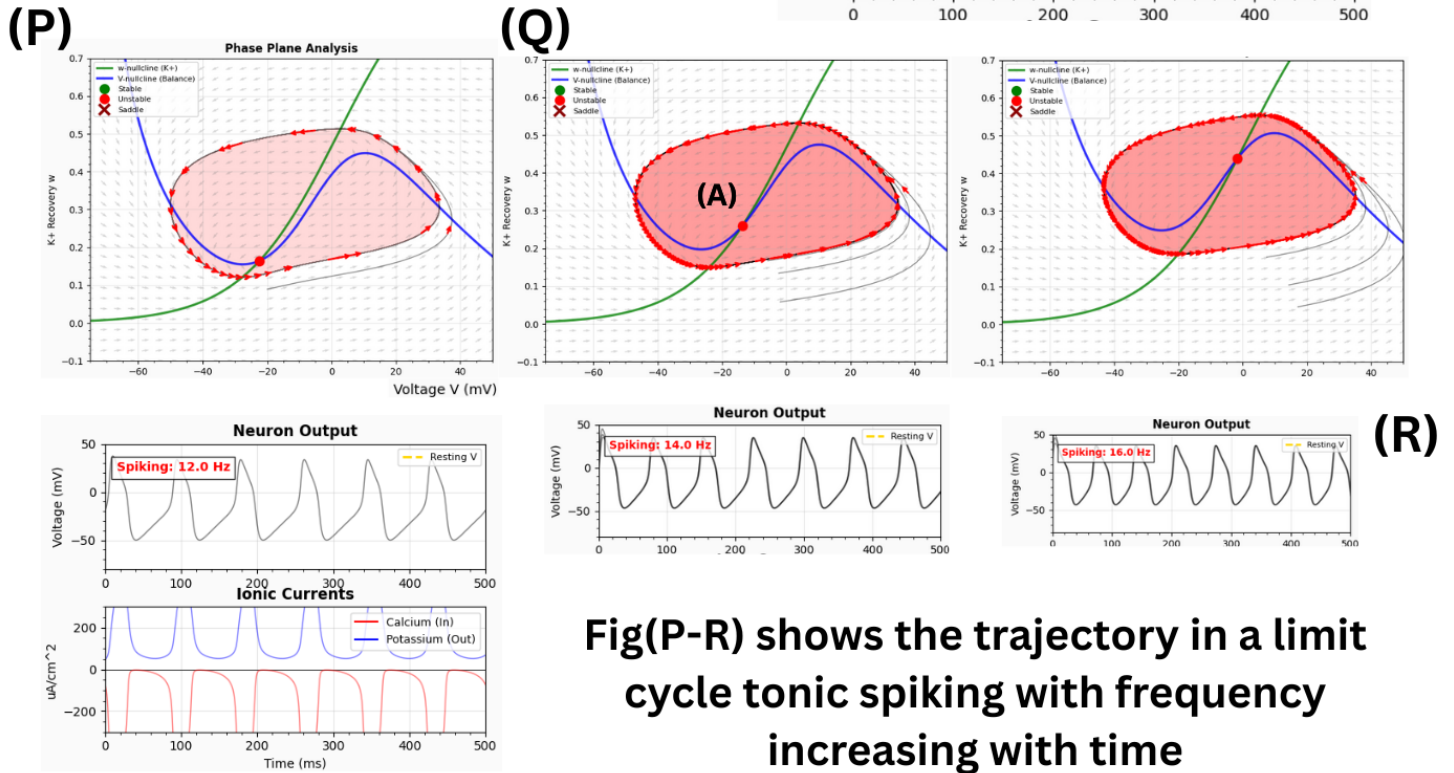
The Morris–Lecar model is a compact, physically interpretable framework widely used to study neuronal coding and dynamics. Its parameters map directly to channel properties, making it useful for investigating rate coding, where stimulus intensity is encoded by firing frequency, and for applying phase–plane methods to quantify the effects of noise (synaptic or intrinsic) on threshold variability and latency jitter.

As a building block for larger systems, coupled Morris–Lecar oscillators reproduce collective phenomena such as synchronized bursting and pacemaker rhythms. Simple parameter manipulations (channel densities, activation curves) allow controlled exploration of how excitability scales during growth or neuromodulation, and how diffuse modulators (e.g., serotonin, dopamine, ACh) may shift global brain states (sleep/wake, attention).

The model also provides a minimal setting for mechanistic hypotheses about computation and pathology. Coexistence of stable resting and spiking states endows neurons with switch- and memory-like behavior relevant to persistent activity and decision-



Fig(A-B) shows the trajectory returning to resting state.



Fig(P-R) shows the trajectory in a limit cycle tonic spiking with frequency increasing with time

Figure 3: Schematic representation of Type 2 dynamics

making. Homeostatic adjustments of conductances can be modeled to maintain target activity levels, while channelopathies are naturally represented by perturbing kinetics or voltage-dependence (e.g., of persistent Na^+ or Ca^{2+} currents), which can induce aberrant subthreshold oscillations or pathological bursting. Importantly, the framework highlights that small, continuous molecular changes often produce discontinuous functional transitions at the cellular or network level, linking biophysics to computation.

In sum, the Morris–Lecar model is “simple in parts, rich in consequence”: its low dimensionality facilitates analysis and

intuition, yet its nonlinear feedbacks capture a breadth of behaviors that presage the even greater diversity found in real neurons with many channel types and intracellular pathways.

2 Introduction to Bursting

The ML model is a deterministic one that predicts whether a neuron will spike or remain at rest based solely on membrane voltage and a set of ionic currents. However, real neurons exhibit far more complex and variable behavior in-vivo than this framework captures. In biological systems, neuronal activity is affected by numerous influences such as: (i) Astrocytic and Microglial modulation. It has been shown that stochastic astrocyte dynamics affect weak signal detection in ML neurons [2]. Even the integration of spatially separated yet integrated synaptic and dendritic inputs contributes to variance. (ii) Omitted variable bias due to the exclusion of important ionic channels, slow gradient accumulation, signaling effects, and other significant parameters restricts the domain of the model. Because of these factors, real neuronal dynamics often deviate from the idealized, noise-free predictions, motivating the use of more detailed or stochastic extensions when biological realism is sought.[1]

Neurons can exhibit different patterns of electrical activity. Besides producing single spikes or a series of regular tonic spiking, some neurons produce bursts—groups of spikes separated by silent periods. Bursting requires the interaction of fast and slow dynamics inside the neuron. The Morris–Lecar (ML) model is originally a 2-dimensional system that can fire spikes. If we add one slow variables, it can also show square-wave and elliptic patterns, and parabolic bursting if two slow variables are added. This slow modulation provides negative feedback that shifts the fast system between spiking and resting states by pushing it across bifurcations, enabling transitions among stable rest, oscillations, and instabilities.

Parabolic bursting is generated without bistability in the fast subsystem and it requires at least two-variables in the slow subsystem. Steady states of the fast subsystem are now represented as an S-shaped surface over the two-dimensional plane of slow variables. Hence they are beyond the current scope

Qualitatively and analytically understand the stochastic noise effects on we also incorporate Gaussian white noise into the voltage equation, simulating the intrinsic variability of ion channel activity and synaptic input in real neurons.

Adapted from -MIT Press: Oscillatory and Bursting properties of neurons - Xiao Wang and John Rinzel

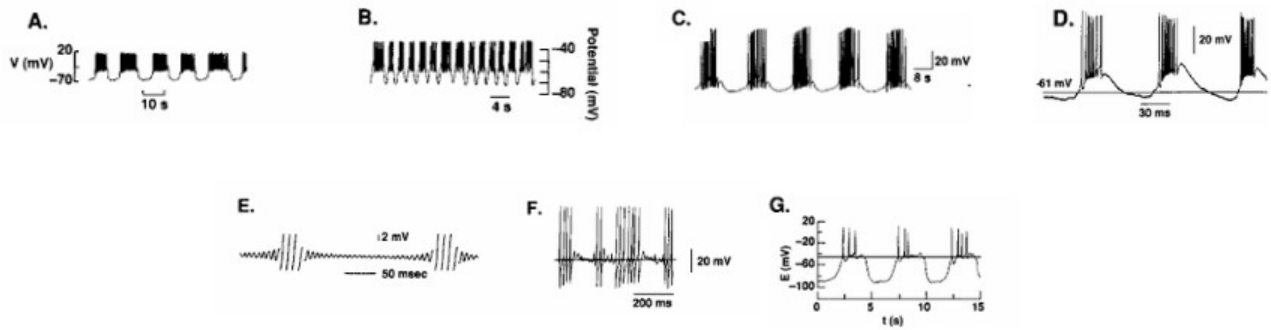


Figure A (Pancreatic beta-cell): Shows square-wave bursting characterized by rapid oscillations on a plateau followed by a silent phase. Spiking is driven by a high-threshold fast calcium current and a slower calcium-activated potassium current.

Figure B (Dopamine-containing neuron): Exhibits elliptic bursting, where the amplitude of oscillations increases and then decreases within each burst.

Figure C (Aplysia R15 neuron): Displays classic square-wave bursting with sharp transitions between the active spiking phase and the silent recovery phase.

Figure D (Cat thalamic reticular neuron): Shows elliptic bursting with characteristic waxing and waning of spike amplitudes.

Figure E (Sepia giant axon): Demonstrates elliptic bursting (often referred to as spindle-like) where oscillations gradually grow from and return to a baseline.

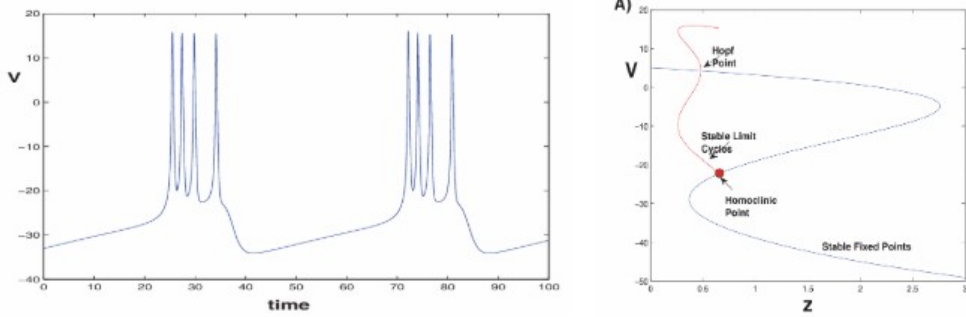
Figure F (Rat thalamic reticular neuron): Exhibits square-wave bursting with distinct, high-frequency spike clusters separated by silent intervals.

Figure G (Rat pituitary gonadotropin-releasing cell): Displays square-wave bursting with a sustained depolarized plateau during the active spiking phase.

Figure 4: Physiologically observed bursting

3 Square-Wave Burster

Square-wave bursting is a well characterised and studied fundamental kind of neuronal excitability characterized by alternating epochs of quiescence (silent phase) and rapid, repetitive spiking (active phase). Mathematically, this behavior arises from a separation of timescales between fast membrane/gating dynamics and a slowly varying modulatory variable, here taken to be



Square-wave bursting. Note that the active phase of repetitive firing is at membrane potentials more polarized than during the silent phase. Moreover, the frequency of spiking slows down at the end of the active phase

Figure 5: Deterministic Square-wave bursting

the intracellular calcium concentration. In this section, I describe the model modifications used, apply a fast-slow decomposition to uncover the geometric mechanisms underlying bursting, and extend the framework to include stochastic perturbations.

We consider a single-compartment conductance-based neuron model with state variables given by the membrane potential V (fast), the potassium activation variable n (fast), and intracellular calcium $[Ca]$ (slow). This yields a three-dimensional dynamical system. Timescale separation is introduced via a small parameter $\epsilon \ll 1$ in the calcium equation. This ensures $[Ca]$ evolves much slower than V and n , allowing for geometric singular perturbation analysis (Fast-Slow analysis). The governing stochastic differential equations (SDEs) are:

$$C_M \frac{dV}{dt} = (I_{app} - I_{ionic}(V, n, [Ca])) dt + \sigma dW_t, \quad (10)$$

$$\frac{dn}{dt} = \phi \frac{n_\infty(V) - n}{\tau_n(V)}, \quad (11)$$

$$\frac{d[Ca]}{dt} = \epsilon (-k_{Ca}[Ca] + \mu I_{Ca}(V)), \quad (12)$$

We change the convention a little to accomodate w for stochastic variables and now consider K^+ gating variable as n where dW_t is a standard Wiener process (Brownian motion) with noise intensity σ , representing intrinsic channel noise or synaptic fluctuations (without loss of generality). In the deterministic limit ($\sigma = 0$), (In the absence of noise) the total ionic current is:

$$I_{ionic} = g_L(V - E_L) + g_K n(V - E_K) + g_{Ca} m_\infty(V)(V - E_{Ca}) + g_{KCa} z([Ca])(V - E_K), \quad (13)$$

with $z([Ca])$ denoting the fraction of active calcium-dependent potassium (KCa) channels, modeled using a Hill function with dissociation constant K_d :

$$z([Ca]) = \frac{[Ca]}{K_d + [Ca]}. \quad (14)$$

The voltage-dependent steady-state activation curves $m_\infty(V)$ and $n_\infty(V)$ are sigmoidal, and $\tau_n(V)$ is the voltage-dependent time constant for potassium activation. Same as before.

The membrane voltage combines all ionic currents and inputs from synapses. Randomness in ion-channel opening, like stochastic gating of Na^+ , K^+ , and Ca^{2+} channels, causes changes in total current that look like noise in the voltage equation.

There are two reasons why this is a common way to estimate conductance-based stochastic modeling:

1. The voltage equation serves as a current equilibrium equation. So changes in total current affect voltage noise directly.
2. When the number of channels is moderately large, noise in gating variables is often fast and roughly Gaussian, which makes a diffusion approximation reasonable. So, the expression σdW_t is also understood as cumulative channel noise.

A small σ means that neurons have a lot of ion channels or are getting weak synaptic bombardment. Intermediate σ causes changes in the timing of spikes and the length of bursts. A big σ can cause burst skipping, early ending, or strange changes between silent and active phases, which can then be extended to noise induced action potentials that may be caused due to resonance.

Even though channel states are random, adding a single noise term to the voltage is a diffusion approximation that shows how the population's fluctuations are averaged. A more in-depth method would add multi-dimensional noise directly to gating variables, which would make the whole system random.

But for bursting models: gating noise is quick, calcium dynamics are comparatively slow and deterministic, and voltage seems to combine noise well. So, the additive voltage noise model is a good choice for studying stochastic bursting because it is commonly used in literature, easy to work with mathematically, and resembles observations to some degree.

3.1 Understanding Geometric Structure

To study the mechanism of bursting, the slow variable $[Ca]$ is treated as a quasi-static bifurcation parameter, denoted c . The *fast subsystem* consists of Equations (10) and (11) with $\sigma = 0$, analyzed for fixed value of z .

Equilibria of the fast subsystem satisfy $dV/dt = 0$ and $n = n_\infty(V)$, forming the V -nullsurface. When projected onto the (V, z) plane, this surface typically exhibits a characteristic Z-shaped curve composed of three branches:

1. **Lower branch:** Stable equilibria corresponding to the hyperpolarized silent phase.
2. **Middle branch:** A saddle-type branch, acting as an unstable separator.
3. **Upper branch:** Depolarized equilibria, often embedded within a region supporting stable periodic spiking (limit cycles).

Square-wave bursting occurs when the slow variable moves the fast subsystem back and forth across a *bistable window*, where a stable equilibrium and a stable limit cycle coexist.

We use a python code to analyse these curves, the method used to study these bursts and their observations are as follows—

Parameter	Square wave	Elliptic
ϕ	0.04	0.067
g_{Ca}	4	4.4
g_{KCa}	0.75	1
V_3	12	2
V_4	17.4	30
E_{Ca}	120	120
E_K	-84	-84
E_L	-60	-60
g_K	8	8
g_L	2	2
V_1	-1.2	-1.2
V_2	18	18
C_M	1	1
I_{app}	45	120
K_{Ca}	1	1
ε	0.1	0.04
μ	0.02	0.01667
$\tau_{g_{CaS}}$	0.05	1

Table 7: Parameter values for Square-wave and Elliptic burster models.

3.2 Methods and Observations

All square wave bursting patterns come in two mathematical forms , first of which is a fold/fold bifurcation and the second is a fold/homoclinic one, in the homoclinic case , we can observe the distinct plateau of stability around the lower branch of the V nullcline, which is the distinctive characteristic feature of this burster seen in fold/homoclinic only which is more biologically relevant fold/fold is rather not observed hence excluded from the study, we simulate it regardless, but the plateau is not very distinctive since it jumps from the resting threshold immediately with little to no pause at all. From observations we can infer that below a certain threshold we see regular spiking (bursting is very parameter sensitive) and within a deterministic limit (with

no noise) we can see the theoretically predicted patterns. Further, there are three methods we use to understand the interactions between variables on the nullclines and trajectory. The first step involves varying only the current for a fixed known z , and no noise. Next we slowly increase the applied current on the system and observe the changes in coefficient of variability (CV) and Interburst interval (IBI). We extrapolate these values from the graph to find out mean time of bursting. In the code, we solve SDE with Euler–Maruyama algorithm. The next step is to find out the effect of the slow variable on the pre-set parameters. We observe that the calcium concentration modulated by z has an effect on the geometric and statistical patterns. We next revert back the slow variability and current to default and vary the noise for different values of current. Each current is run in three trials; the diagrams elucidate the first of the three runs. the remaining two runs were conducted to ensure that there was consistency in the results and that locally produced stochasticity could be averaged out to understand behavior. The interpretations of these observations accompany their phase plane diagrams. The data obtained is tabulated neatly below.

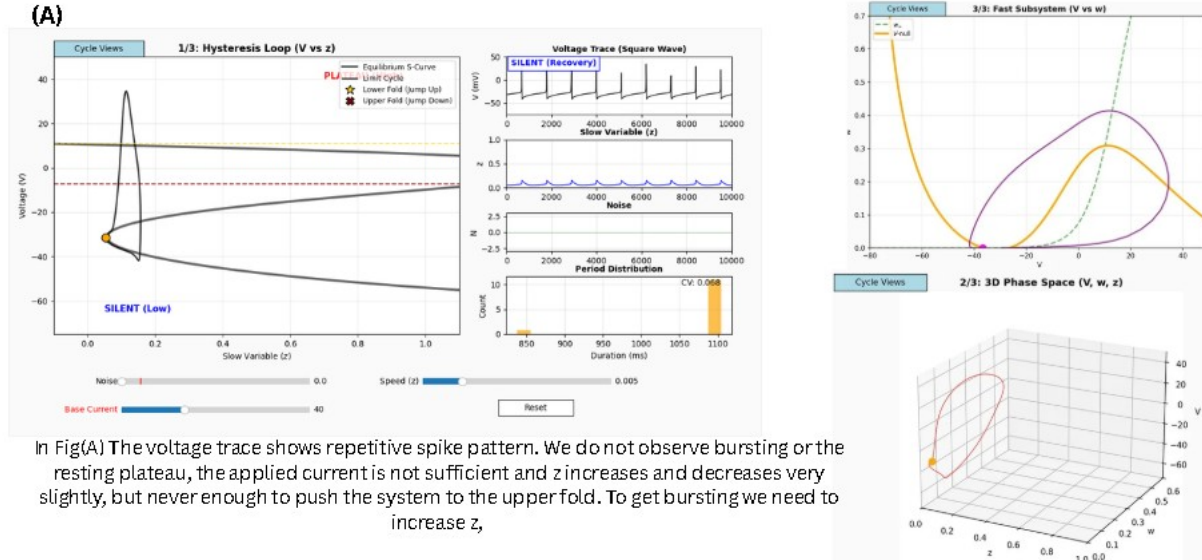


Figure 6: Non-activation of bursting. The ISI histogram shows a single narrow peak with a low CV (0.09), indicating highly regular tonic spiking.

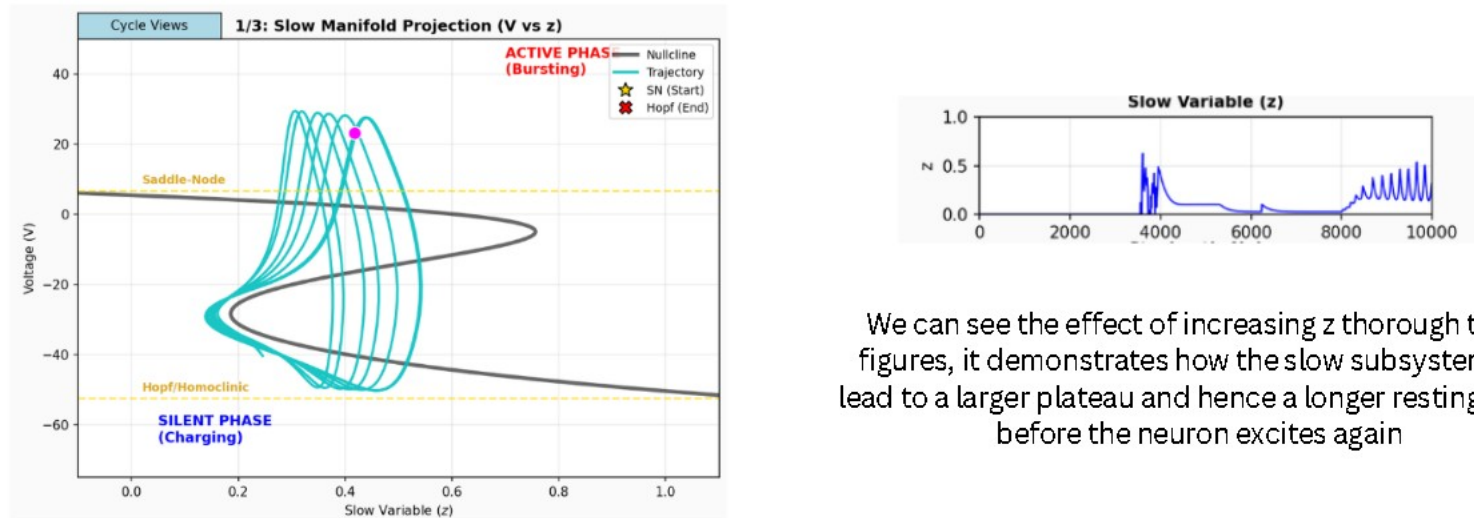
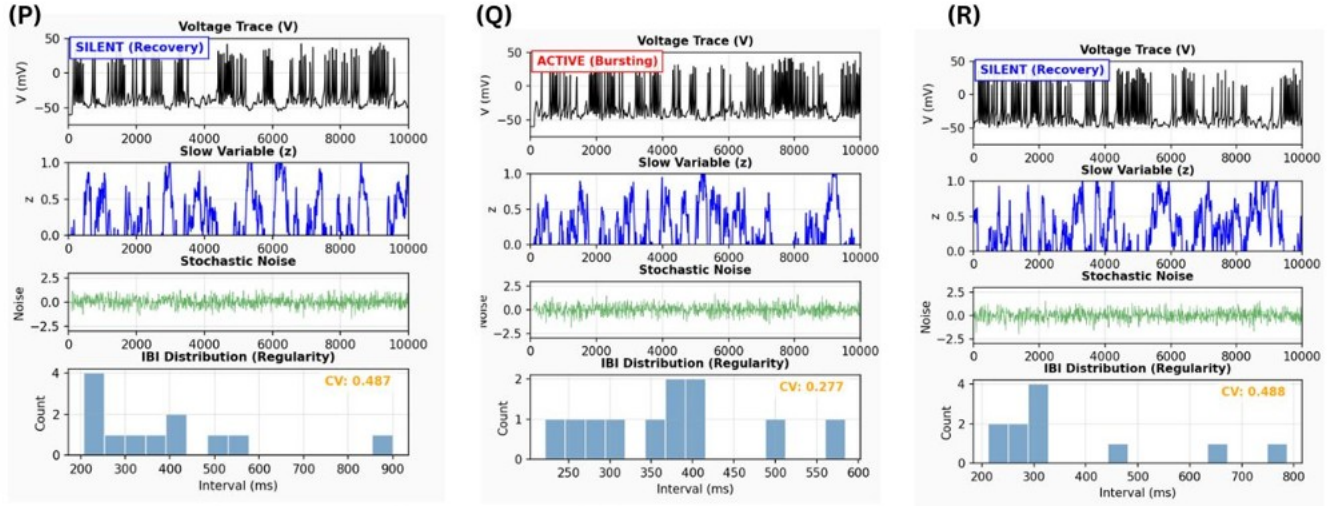


Figure 7: Increasing values of ' z ' leads to a longer trajectory spanning the plateau



This non-monotonic CV vs. current behavior is theoretically expected near bifurcation boundaries.
Using CV as a proxy for burst regularity

In Fig(P) For $\sigma=0.5$ and $z=0.005$ at 45mA

Voltage trace shows intermittent spike clusters separated by silent phases, characteristic of square-wave bursting.

Noise perturbs timing but does not destroy the burst structure.

Broad IBI distribution and moderate CV (~0.49) indicate irregular burst timing. In all of our trials the IBI was consistently above 0.400. In some trials outside of this testing we had outliers below 0.400 also.

Thus, the neuron shows mean (average) square-wave bursting, where bursting emerges in time-averaged statistics rather than as a precise deterministic rhythm.

In Fig(Q) For $\sigma=0.5$ and $z=0.005$ at 50mA

Voltage trace shows sustained bursting with shorter and more consistent silent gaps, indicating the system is firmly in the active bursting regime.

The IBI distribution is narrower and the CV is lower, showing more regular and stable bursting compared to the recovery/mean bursting case. In our 5 trials the CV obtained were- 0.277, 0.348, 0.341, 0.369, 0.406. With a mean of 0.348.

At higher current but we can still qualitatively see order within disorder.

In Fig(R) For $\sigma=0.5$ and $z=0.005$ at 55mA

Voltage trace shows bursting

The IBI distribution is broader and the CV is higher in the range of (0.400-0.500) showing more irregularity compared to the previous case- the CV obtained in our trials are- 0.488, 0.511, 0.496, 0.493, 0.433. With a mean of 0.484.

At higher current, the system approaches the upper boundary of the bursting regime, where excessive excitation and noise lead to irregular burst termination.

Figure 8:

4 Elliptic Burster

In several brain areas, neurons have been observed experimentally to engage in a rhythmic pattern of behavior referred to as elliptic bursting. In elliptic bursting, neuronal activity alternates between active phases, characterized by large amplitude oscillations, and quiescent phases, associated with oscillations of much smaller amplitudes. Neuronal examples are given in the context of thalamic sleep rhythms and in cat and snail models as in the examples listed earlier.

To get Elliptic Bursting in this model, we typically need parameters as described in the table at the start of the section, which somewhat resemble Type-II parameters. (where the onset of spiking is a Hopf bifurcation rather than a Saddle-Node). In the Fast-Slow analysis, the bifurcation diagram of the Elliptic Burster has a different geometric structure. There is usually a single straight curve of equilibrium points plotted on the V v/s z plot reduced for fast-slow analysis, although the simulations we run also include the 3D space so we can appreciate the geometry of the trajectory. As the slow variable (Calcium) changes, this equilibrium line passes through two Hopf Bifurcation points. Between the points: The steady state is unstable (Unstable Focus). Outside the points: The steady state is stable (Stable Focus). There is a "Bubble" of Cycles: A branch of limit cycles that connects these two Hopf points. This looks like a balloon or bubble attached to the equilibrium line. We visualise these limit cycle oscillations as " elliptic spindle " spikes. A critical theoretical concept in elliptic bursting is "**Slow Passage through a Hopf Bifurcation**," often referred to as the **Memory Effect**

There are three stages: **Delayed Stability Loss:** When the slow variable drifts the system past the first Hopf point, the system does not spike immediately. It "tracks" the now-unstable equilibrium for a period because it was stable a moment ago. **The Spindle Formation:** Microscopic noise eventually amplifies these unstable forces, causing oscillations to grow exponentially from infinitesimally small amplitudes—creating the characteristic "waxing" side of the spindle. **Termination:** As the slow variable approaches the second Hopf point, the limit cycle shrinks back down until the system settles into a stable equilibrium, creating the "waning" effect.

4.1 Classification: Hard vs. Soft Elliptic Bursting

The transition into and out of the limit cycle "bubble" determines whether the bursting is perceived as smooth (Soft) or an abrupt jump (Hard).

Feature	Soft Elliptic Bursting	Hard Elliptic Bursting
Transition	Continuous (Supercritical)	Discontinuous (Subcritical)
Bifurcation	Supercritical Hopf	Subcritical Hopf
Amplitude	Grows gradually from zero	Jumps abruptly to large value
Hysteresis	Absent (No bistability)	Present (Bistability exists)
Onset	Oscillations emerge smoothly	Sudden onset of full spikes

Table 8: Differences between soft and hard elliptic bursting.

Biological Significance and Noise Sensitivity—Elliptic bursting serves specific functional roles that distinguish it from square-wave pacemakers:

- **Sleep Spindles:** Generated in the Thalamus during NREM sleep, these 10-15 Hz oscillations facilitate memory consolidation and provide sensory shielding.
- **Frequency Resonance:** Type II neurons act as biological resonators tuned to specific frequencies (e.g., Gamma or Theta), allowing them to filter out asynchronous noise.
- **Motor Control:** The gradual "waxing and waning" amplitude allows for smoother recruitment of muscle fibers in Central Pattern Generators (CPGs).
- **Noise Sensitivity:** Unlike the "timing jitter" of square-wave bursting, elliptic bursting is prone to **Envelope Destruction**. High noise levels can eliminate the "Hopf Delay," causing the burst to start prematurely and destroying the smooth spindle shape.

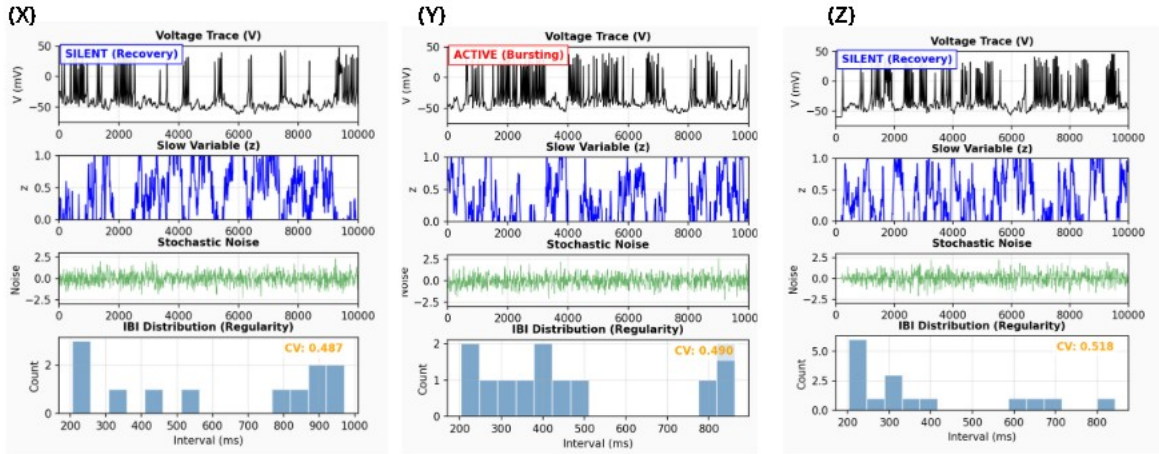
5 Appendix

For more details, see [Github page with explanatory code](#)

Images generated using : [Biorender](#)

References

- [1] T. Azizi and B. Alali. Impact of chloride channel on spiking patterns of morris–lecar model. *Applied Mathematics*, 11:650–669, 2020. Licensed under CC BY 4.0.
- [2] Erdem Erkan. Signal encoding performance of astrocyte-dressed morris–lecar neurons. *Chaos, Solitons & Fractals*, 177:114223, 2023.
- [3] G. Bard Ermentrout and David H. Terman. *Mathematical Foundations of Neuroscience*, volume 35 of *Interdisciplinary Applied Mathematics*. Springer, 2010.
- [4] Eugene M. Izhikevich. *Dynamical Systems in Neuroscience: The Geometry of Excitability and Bursting*. MIT Press, Cambridge, MA, 2007.
- [5] Catherine Morris and Harold Lecar. Voltage oscillations in the barnacle giant muscle fiber. *Biophysical Journal*, 35(1):193–213, 1981.
- [6] John Rinzel and G. Bard Ermentrout. Analysis of neural excitability and oscillations. In Christof Koch and Idan Segev, editors, *Methods in Neuronal Modeling*, pages 135–169. MIT Press, Cambridge, MA, 1989.
- [7] Kunichika Tsumoto, Hiroyuki Kitajima, Tetsuya Yoshinaga, Kazuyuki Aihara, and Hiroshi Kawakami. Bifurcations in morris–lecar neuron model. *Physica D: Nonlinear Phenomena*, 211(1–2):1–15, 2005.



In Fig(X) For $\sigma=0.7$ and $z=0.005$ at 45mA

Voltage trace shows bursting, but noise is now comparable to the slow-fast drive, intermittently pushing the system across bifurcation boundaries.

The trials show an increase in the CV now in the range of (0.45–0.6). Our observations being -0.527, 0.458, 0.498, 0.629, 0.425 with a mean of -0.507.

In Fig(Y) For $\sigma=0.7$ and $z=0.005$ at 50mA

Voltage trace shows spike clusters separated by silent phases, but the bursts are highly irregular and variable in duration, previously the bursting was more regular.

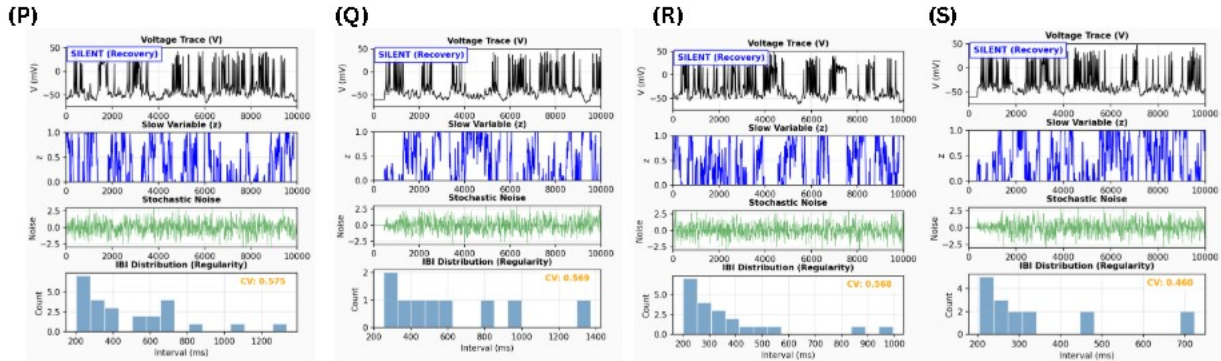
The trials show an increase in the CV now in the range of (0.45–0.6). Our observations being -0.420, 0.527, 0.462, 0.477, 0.490 with a mean of -0.475.

In Fig(Z) For $\sigma=0.7$ and $z=0.005$ at 55mA

Voltage trace shows noise-influenced square-wave bursting. Even at high noise, the exact spike/burst timing can fluctuate between trials. Some trials may accidentally produce more regular bursts due to short sampling time

The trials show an increase in the CV>0.5. Our observations being -0.518, 0.611, 0.488, 0.490, 0.570 with a mean of -0.535.

Figure 9:



In these three figures we use $\sigma=0.102$ and vary currents between 35mA(sub-threshold), 45mA, 50mA and 55mA.

Even with a sub threshold current we can see some kind of bursting (although highly irregular) the noise "kicks" the system across the Saddle-Node (SN) bifurcation threshold into an active state that it wouldn't otherwise reach.

As current increases to 45mA and above, the system enters the deterministic bursting regime. While the noise continues to cause variability, the slight downward trend in CV suggests that higher base currents provide a stronger deterministic drive. At high current like at 55mA it may cause immature termination due to noise.

Figure 10: Affect of noise on increasing current

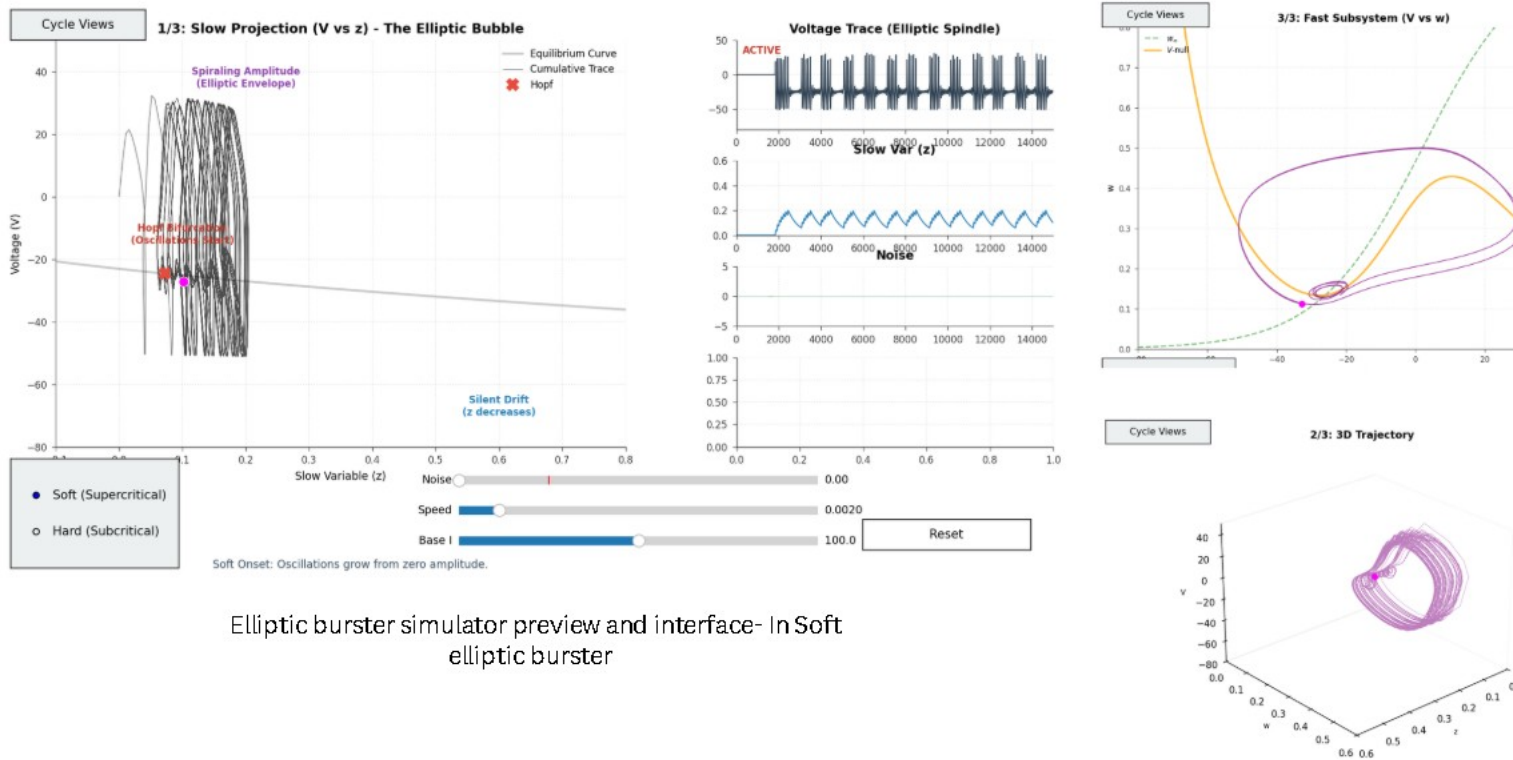


Figure 11: Soft elliptic bursting

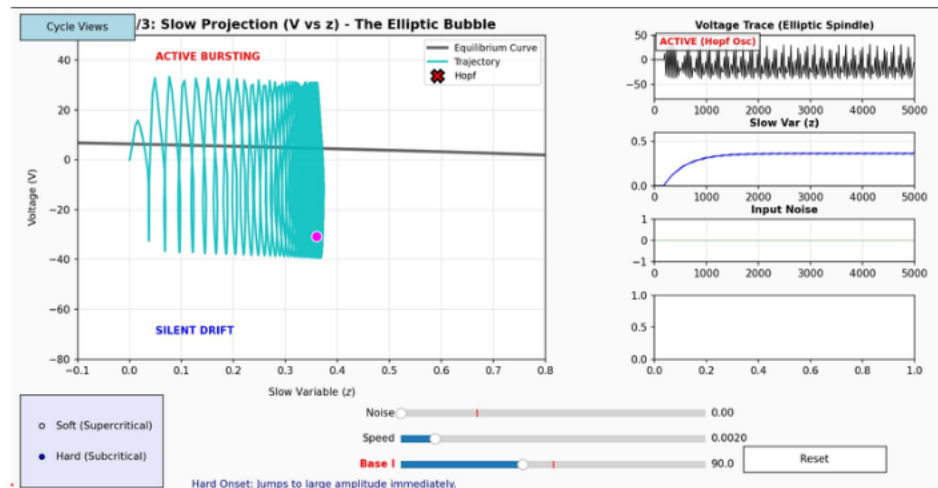


Figure 12: Hard elliptic bursting

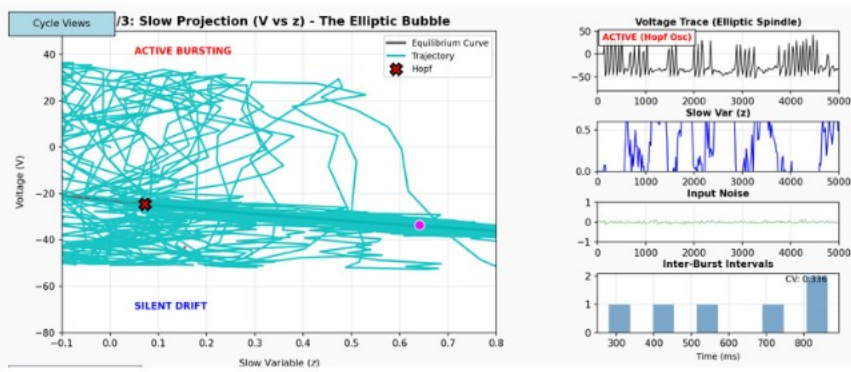
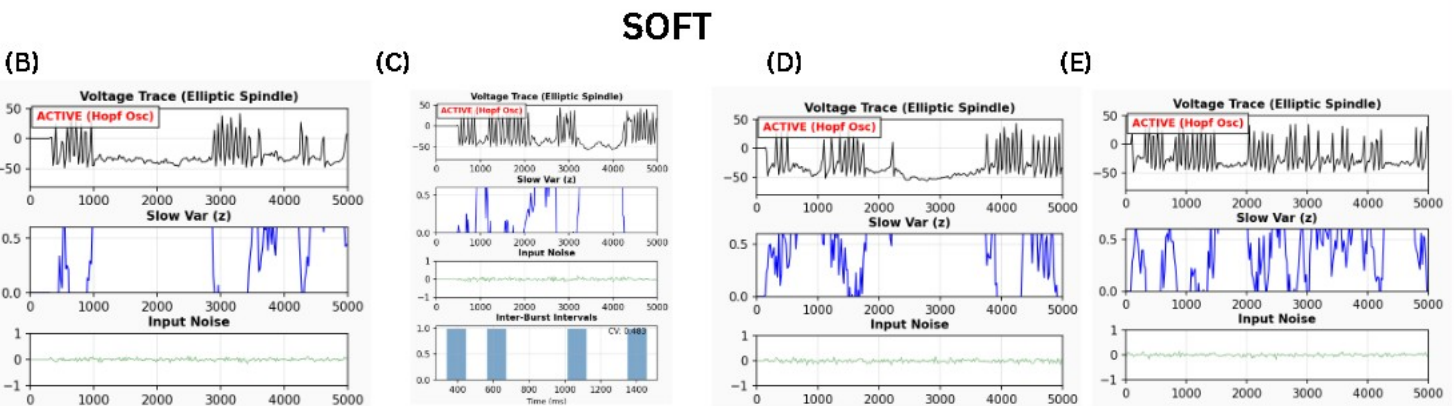


Figure 13: Base case

In Fig(A) For sigma=0.5 and z=0.002 at 100mA

Voltage trace shows elliptic bursting but noise is disturbs the otherwise regular trace, regardless it is deterministically dominant atleast at this current and noise.

For all other trials only the voltage trace and observations shall be reported.



In Fig(B) For sigma=0.5 and z=0.002 at 120mA

In Fig(C) For sigma=0.7 and z=0.002 at 100mA

In Fig(D) For sigma=0.7 and z=0.002 at 120mA

In Fig(E) For sigma=0.5 and z=0.004 at 120mA

Shows elliptic bursting with visible interference from noise. The slow variable z shows distinct peaks corresponding to the active bursting phases, but the rhythm is irregular.

Despite a lower current, the higher noise creates significant "trial-to-trial" variation. The Inter-Burst Intervals (IBI) plot shows a high Coefficient of Variation (CV: 0.483), indicating highly random timing between bursts.

With the higher current the bursting becomes very fragmented. The noise prominently disrupts the spindle formation, making the active phases look "jittery" or less defined compared to lower noise trials.

Increased Slow Variable Baseline: By doubling z to 0.004, the frequency of the bursts appears to increase. However, the noise still prominently disturbs the voltage trace, leading to huge variations in activity across different trials.

For all other trials only the voltage trace and observations shall be reported.

Figure 14: Observations from soft bursting

The "Soft" cases use a supercritical Hopf, where the limit cycle (spiking) emerges with zero amplitude and grows. "Hard" cases use a subcritical Hopf, where a large-amplitude limit cycle appears as soon as the trajectory starts off.

In the Hard regime, noise is more likely to cause "all-or-nothing" transitions. In the Soft regime, noise primarily "disturbs" the existing small oscillations, creating the jittery, irregular "spindles" seen in traces D and E.

HARD

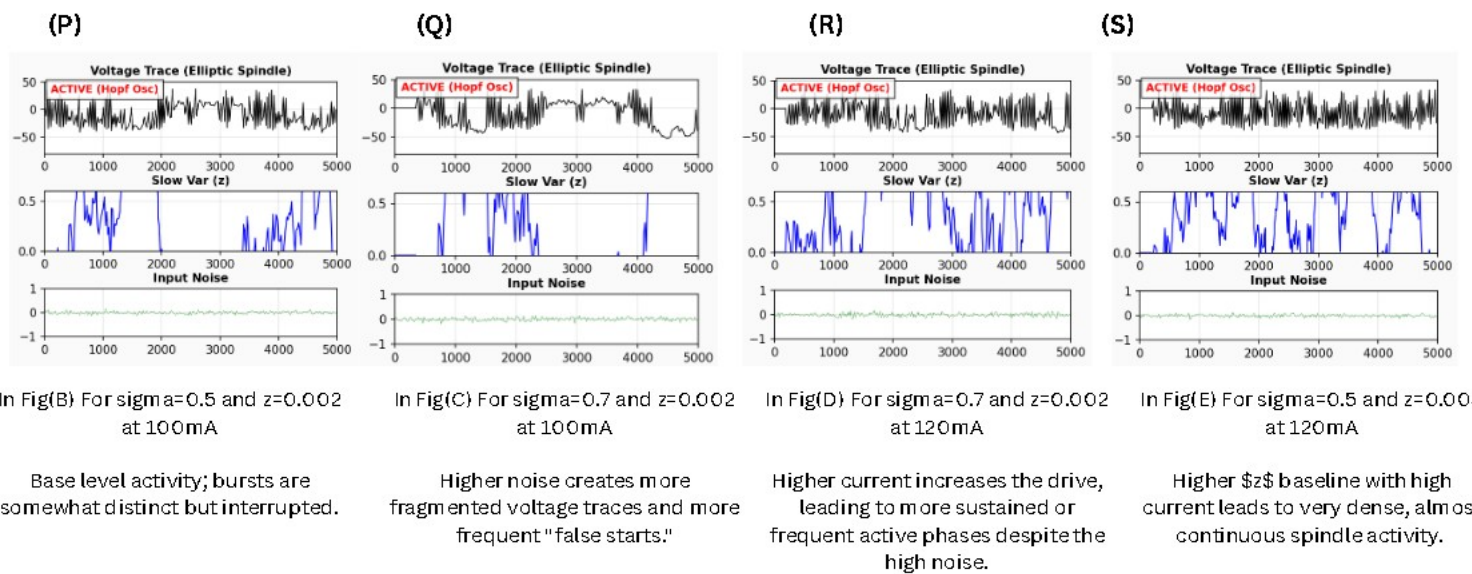


Figure 15: Observations from hard bursting